SIMULATION OF ENERGY HARVESTING EEL BY THE IMMERSED BOUNDARY METHOD

Ki Sung Jung,[1] Wei-Xi Huang[1] and Hyung Jin Sung[*2]

In the present study, we carry out numerical simulations of energy harvesting eel by using the immersed boundary method. Eel is modeled by a flexible filament and is placed behind a circular cylinder. We perform systematic simulations in order to explore the effects of Reynolds number. The instantaneous eel motion is analyzed under different conditions and surrounding vortical structures are identified. The flapping frequency of eel has been compared with that in case of plate alone as well as filament alone. As increasing Reynolds number, we can see that the flexible filament flaps passively by obtaining the Strouhal number of cylinder alone and filament with cylinder.

Key Words : Energy Harvesting Eel, Immersed Boundary Method, Numerical Simulation

1. INTRODUCTION

Most fishes live in habitats where they usually encounter vortices induced by fluid flow past stationary objects or by the propulsive movements of other fishes. The dynamics of swimming fish has a complicated interaction between their deformable shapes and the surrounding fluid flow. Simulations and experiments for realizing interactions between a flow and a deformable body are difficult to perform because of the challenge of flow visualization and three dimensional flow effects[1].

Zhang et al.[2] used flexible filaments immersed in a flowing soap film to imitate the undulatory propulsion motions of a fish. They observed two distinct stable states, i.e. the stretched-straight state and the self-sustained flapping state. Numerical simulations on the interaction between deformable body and the surrounding fluid flow were also carried out. Zhu & Peskin [3] simulated in case of a filament and two side by side filaments for comparison with Zhang et al.'s experiment using the immersed boundary method. Huber[4] reported that the vortices trailing the flapping thread are much smaller than the size of each 'flap', unlike the vortices created by a disc or a swimming fish, which are comparable to the size of the body. Huang et al.[5] also observed the trend in the flow pattern with increasing Reynolds number is consistent with the experimental results of Zhang et al.[2], which showed that a procession of small vortices is produced at high Reynolds number.

Liao et al.[6] studied the locomotion of a live trout in the wake of a D cylinder, revealing that the trout adopt a novel mode of locomotion to slalom smoothly through the Karman vortex street shedding from the D cylinder. In contrast to free-swimming fish, fish using the von Karman gait only activate the most anterior part of their swimming muscles. This indicates that their body motion is generated passively by interaction with the oncoming flow of water. The electromyography demonstrates reduced muscle activity and conversed energy in this locomotion compared to that in free swimming. Jia & Yin[7] observed that when two filaments are arranged in tandem, the frequency of the downstream filament and upstream filament is the same, but the amplitude of downstream filament is larger than that of upstream filament. The downstream filament indeed extracts energy from the vortex street. Energy capture from environmental vortices can be explained as a hydrodynamic mechanism to improve the performance of swimming fishes. The reduced muscle activity is the first direct evidence for the energy-saving benefits of swimming in a wake. Explaining a relation between vortex

1 한국과학기술원 기계공학과
2 정회원, 한국과학기술원 기계공학과
* Corresponding author, E-mail: hjsung@kaist.ac.kr

interaction and reduced muscle activity may provide insight into the dynamics and evolution of aggregation in moving animals. In addition, an exact understanding of the interactions between vortices and reduced muscle activity has a possibility to aid in design of a fish pathway.

The small amount of power demanded by most current electronic devices has a possibility to convert the energy in environment into electric energy. Batteries are the power source used in most devices but the disadvantage of batteries is the need to either replace or recharge them periodically. An alternative to batteries is harvesting energy from the circumstances. Recently, most people have been focused on bio-inspired device. Energy harvesting eel is one of bio-inspired devices, which is a system for converting the flow energy, usable boundlessly in regions containing flowing water, to electric power. For generating the power, an eel uses the Karman vortex street induced in the wake of a bluff body. This device can be used to charge batteries of capacitors of remote sensor[8,9].

Taylor et al.[8] showed that the experiment using piezoelectric polymers was carried out in case of different Reynolds numbers. Experimentally, the strain is calculated by recording the curvature of an eel in a flow tank and electrically by measuring the open circuit voltage of the eel segment electrodes. The resulting strain on the piezoelectric polymer generates a low-frequency ac voltage signal along the electroded segment, which is converted into dc for charging the storage battery of the remote sensor. There is an ideal coupling where the flapping frequency matches the shedding frequency. In Allen et al.[9], the energy harvesting eel has been experimentally examined by using frequency response measurements and PIV, and a filament showed lock-in behavior in the wake of a bluff body. When the filament reaches lock-in status, its wavelength and amplitude are almost similar to the undisturbed vortex street.

In the present study, we perform systematic simulations in order to explore the effects of Reynolds number. Numerical simulations of energy harvesting eel by using the immersed boundary method are carried out. Eel is modeled by a flexible filament and is placed behind a circular cylinder. The interaction between eel and vortical structures shedding form the cylinder is studied.

2. NUMERICAL METHOD

2.1 PROBLEM FORMULATION

The fluid motion is described by Eulerian variables defined on a fixed cartesian mesh, while the immersed boundary motion is described by Lagrangian variables defined on a freely moving mesh. The Eulerian and Lagrangian variables are connected by a smoothed approximation of the Dirac delta function.

The unsteady viscous fluid flow is governed by the Navier-Stokes equations and the continuity equation.

$$\rho_f\left(\frac{\partial u}{\partial t}+u \cdot \nabla u\right) = -\nabla p+\mu\nabla^2 u+f \tag{1}$$

$$\nabla \cdot u = 0 \tag{2}$$

where u=(u,v) is the velocity vector, p is the pressure ρ_f is the fuid density, μ is the dynamic viscosity, and f is the momentum forcing applied to enforce the no-slip boundary condition along the immersed boundary on the fluid.

The governing equations for an inextensible eel are written in a Lagrangian form. The motion equations and inextensibility condition are

$$\rho_1 \frac{\partial^2 X}{\partial t^2} = \frac{\partial}{\partial s}\left(T\frac{\partial X}{\partial s}\right) - \frac{\partial^2}{\partial s^2}\left(\gamma\frac{\partial^2 X}{\partial s^2}\right)+\rho_1 g - F$$

$$\frac{\partial X}{\partial s} \cdot \frac{\partial X}{\partial s} = 1 \tag{4}$$

where X denotes the eel position, T denotes the tension force along the eel axis, γ denotes the bending rigidity, F denotes the Lagrangian forcing exerted on the eel by the surrounding fluid, ρ_1 denotes the line density of eel, g denotes the gravity force. From Eq. (3) and (4), the Poisson equation for T can be expressed as

$$\frac{\partial X}{\partial s} \cdot \frac{\partial^2}{\partial s^2}\left(T\frac{\partial X}{\partial s}\right) = \frac{1}{2}\frac{\partial^2}{\partial t^2}\left(\frac{\partial X}{\partial s} \cdot \frac{\partial X}{\partial s}\right) -$$
$$\cdots \frac{\partial^2 X}{\partial t \partial s} \cdot \frac{\partial^2 X}{\partial t \partial s} - \frac{\partial X}{\partial s} \cdot \frac{\partial}{\partial s}(F_b - F) \tag{5}$$

where $F_b = -\partial^2/\partial s^2(\gamma\,\partial^2 X/\partial s^2)F_b$ denotes the bending force. Although the first term on the right hand side of above equation is originally zero because of the inextensibility condition, we left for numerical errors of the inextensibility

constraint. At the free boundary, we have

$$T=0,\ \frac{\partial^2 X}{\partial s^2}=(0,0),\ \frac{\partial^3 X}{\partial s^3}=(0,0). \tag{6}$$

At the fixed boundary, we use the simply supported condition,

$$X=X_0,\ \frac{\partial^2 X}{\partial s^2}=(0,0). \tag{7}$$

The time-discretized eel motion equation is written as following.

$$\frac{X^{n+1}-2X^n+X^{n-1}}{\triangle t^2}=RHS^{n+1}-F^n \tag{8}$$

where the superscript n denotes the nth time step, $\triangle t$ denotes the time increment, and RHS denotes the tension force and the bending force and the gravity force term for simplicity. To get the desired position of the immersed boundary at the next time step, the momentum forcing term can be given by

$$F^n=-\frac{\widetilde{X_{ib}^{n+1}}-2X^n+X^{n-1}}{\triangle t^2}+RHS^{n+1} \tag{9}$$

where $\widetilde{X_{ib}^{n+1}}$ denotes a estimation of the new position of the fluid point initially aligned along the IB. In other words, the momentum forcing in Eq.(9) forces the immersed boundary points to move with surrounding fluid points. $\widetilde{X_{ib}^{n+1}}$ is indicated by

$$\widetilde{X_{ib}^{n+1}}=X_{ib}^n+U_{ib}^n\triangle t \tag{10}$$

where X_{ib}^n is the position of the fluid point at the present time step and U_{ib}^n is the fluid velocity interpolated at the lagrangian point X^n.

We observed that the coefficient $-1/\triangle t^2$ in Eq. (9) becomes very large because $\triangle t$ is generally given a small value. The first term on the right hand side of Eq. (9) works essentially as a feedback function. Small variation of $\widetilde{X_{ib}^{n+1}}$ may induce large change in $-(\widetilde{X_{ib}^{n+1}}-2X^n+X^{n-1})/\triangle t^2$. Thus, we neglect RHS^{n+1} in Eq.(9). and relax the coefficient of the term $-(\widetilde{X_{ib}^{n+1}}-2X^n+X^{n-1})/\triangle t^2$,

$$F^n=k(\widetilde{X_{ib}^{n+1}}-2X^n+X^{n-1}) \tag{11}$$

where k is a large negative constant. After getting the lagrangian momentum forcing term, we transform it to the eulerian form by the Dirac delta function.

$$f^n(x,t)=\rho\int F^n(s,t)\delta(x-X(s,t))ds \tag{12}$$

where $\rho=\rho_1/\rho_f L_r$ comes from non-dimensionalization. The interpolation of velocity is expressed as

$$U_{ib}^n(s,t)=\int u^n(x,t)\delta(X(s,t)-x)dx \tag{13}$$

2.2 NUMERICAL ALGORITHM

In the present simulations, the computational domain for energy harvesting eel is a rectangle, and a uniform flow moves from the left side to the right side of the computational domain, as shown in Fig 1. Dirichlet boundary conditions ($u=U_\infty, v=0$) are used at the inflow and fir-field boundaries, and a convective boundary condition is used at the outflow. The conputational domain is -8D<x<24D and -16D<y<16D, and the grid size is 1024×370 in the streamwise(x) and transverse(y) directions. 32 grid points are uniformly distributed inside the cylinder in both the x direction and y direction and grid is stretched outside of -3D<y<3D. h denotes the mesh size and a mesh of uniform size is distributed around the immersed boundary in the x direction and y direction. h=△x=△y=D/32. Time step is 0.002. Fig.1 indicates the significant simulation parameters involved in describing the behavior of the energy harvesting eel. U_∞ denotes the free-stream velocity, D denotes the width of the circular cylinder and s denotes the distance between the circular cylinder and the fore part of filament and L denotes the filament length.

In the present study, the discretized Navier-Stokes equations are solved by the fractional step method on a staggered Cartesian grid. The velocity components and momentum forcing are defined on the staggered grid, whereas the pressure is applied at the centers of cells. Fully implicit time advancement

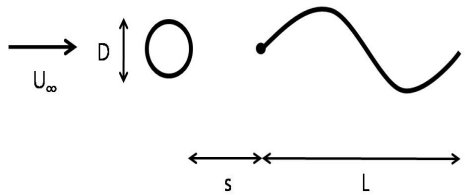

Fig. 1 Schematic of energy harvesting eel

is employed, with the Crank-Nicholson scheme being used for the discretization of the diffusion and convection terms. Decoupling of the velocity and pressure is achieved by block LU decomposition in conjunction with approximate factorization. Details of the approximate factorization are able to be found in Kim et al.[10]. Due to the implicit treatment of the nonlinear convection terms, further decoupling of the intermediate velocity components is made and finally a system of tridiagonal matrices is formed instead of a large sparse matrix. The momentum equation is solved without iteration and the computational cost is reduced significantly. The pressure Poisson equation is solved by a direct method using FFT or a multigrid method. The pressure is then used to correct the velocity field to satisfy the continuity equation.

$$\frac{u^* - u^n}{\triangle t} + N^* = -Gp^{n-1/2} + \cdots \frac{1}{2Re}(Lu^* + Lu^n) + f^n + mbc, \tag{14}$$

$$\triangle t DG\delta p = Du^* - cbc, \tag{15}$$

$$u^{n+1} = u^* - \triangle t G\delta p, \tag{16}$$

$$p^{n+1/2} = p^{n-1/2} - \delta p. \tag{17}$$

where N denotes a linear operator for the convective term, L represents the discrete Laplacian viscous operator, G is the discrete gredient operator and D is the discrete divergence operator, respectively.

The whole process of the present numerical algorithm for simulating the energy harvesting eel is summarized as follows:

(1) At the nth time step, we know the fluid velocity field u^n and the eel positions X^n and X^{n-1}. Interpolate the fluid velocity at the immersed boundary to obtain U_{ib}^n by Eq.(13), and then calculate the Lagrangian interaction force F^n by Eq. (11).

(2) Spread the Lagrangian interaction force to the Eulerian grid by using Eq. (12). Solve Eq. (14)-(17) to obtain the updated fluid velocity field and pressure field.

(3) Calculate the tension force at the intermediate time step $T^{n+1/2}$ by Eq. (5). Solve Eq. (3) to obtain the eel position at the new step X^{n+1}. This ends one time step marching.

More details about the numerical method can be found in Huang et al. [5,11].

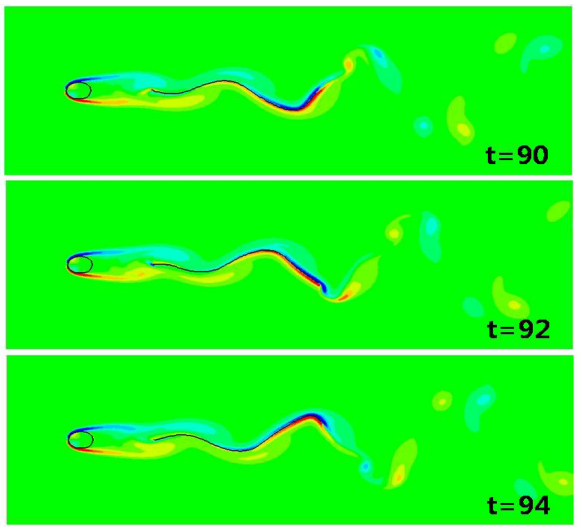

Fig. 2 Instantaneous vorticity contours of energy harvesting eel at Re= 200, s=3D and L=8D at three successive times

3. Numerical Results

In our simulation, we select a filament with length of L=8D, which is placed behind the cylinder with a distance of s=3D. Fig. 2 shows the instantaneous vorticity contours at Re=200 at three successive times. The vortex behind the cylinder is not detached from the cylinder before encountering the filament at Re=200. We can see the vortical structures convecting along the length of the filament. When the Reynolds number is increased at Re=500 as shown in Fig. 3, the vortex is shedding from the cylinder and becomes stronger. As increasing Reynolds number, the vortex size decreases and behind the filament, the number of vortices shedding from the filament during a flapping period increases. The amplitude for Re=200 is small at the fore part and is gradually increased. The flapping at Re=500 is more energetic with the larger amplitude for the fore part. Fig. 4 shows superimposed images of the flapping filament motion over a flapping cycle. The amplitude of the fore part at Re=200 is

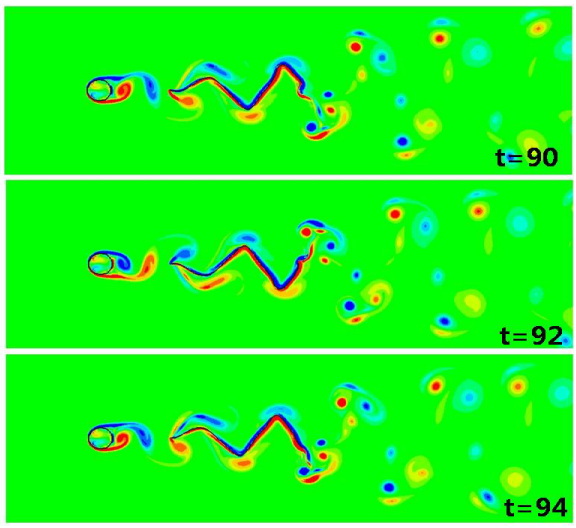

Fig. 3 Instantaneous vorticity contours of energy harvesting eel at Re=500, s=3D and L=8D at three successive times

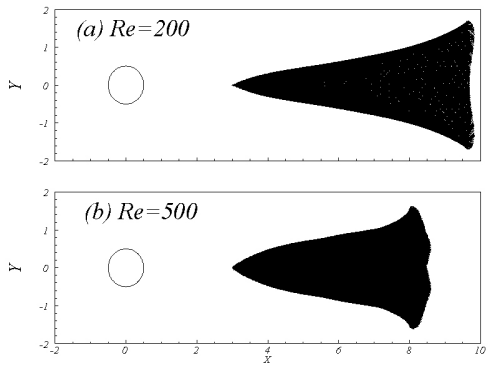

Fig. 4 Superposition of the eel positions during a flapping cycle(a) Re=200; (b) Re=500

smaller than that compared with Re = 500. The amplitude of the rear part at Re = 500 is almost the same as that of the rear part Re = 200. Fig. 5 presents time history of free end position and midpoint position at Re = 200 and Re = 500. The filament is flapping uniformly in the y-direction. Transient time at Re = 500 is longer than that at Re = 200. We can see that the frequency of midpoint is the same as that of free end but there is a phase difference between midpoint and free end.

Fig. 6 shows time history of the lift coefficient of the filament and cylinder at Re = 200 and Re = 500. After the vortex shedding is established, the lift coefficient changes with respect to time at a single frequency. The frequency of the filament and cylinder is same because the filament is passively flapping using the vortex induced by the cylinder. The magnitude of lift coefficient at Re = 500 is larger than

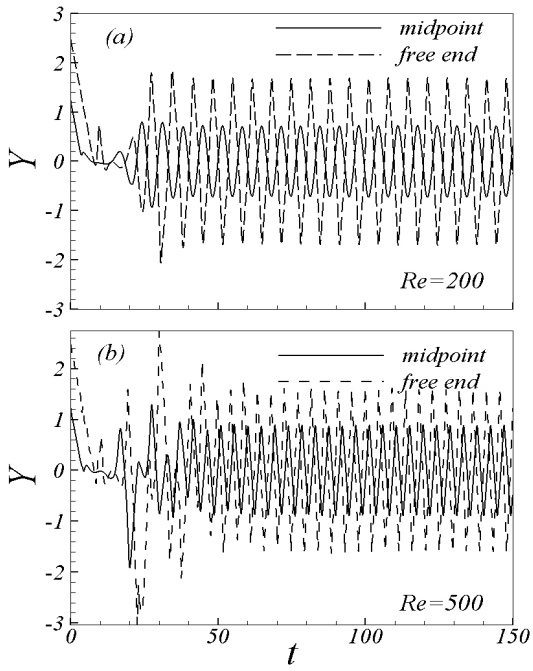

Fig. 5 Time history of the midpoint and free end position at (a) Re=200; (b) Re=500

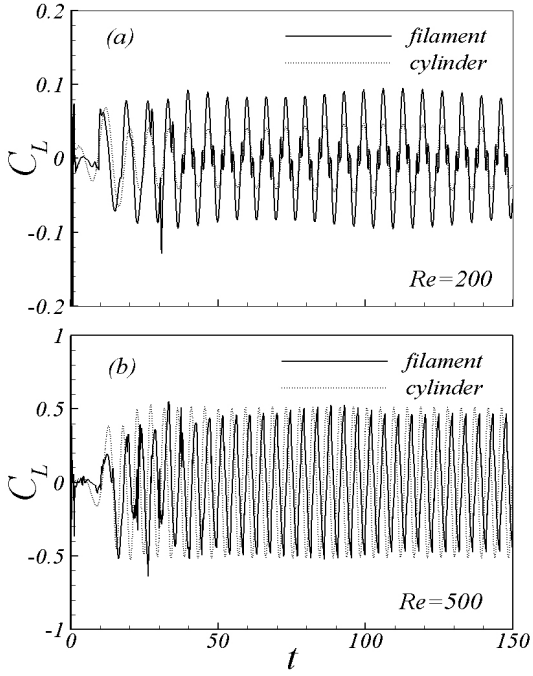

Fig. 6 Time history of the lift coefficient of the filament and cylinder at (a) Re=200; (b) Re=500

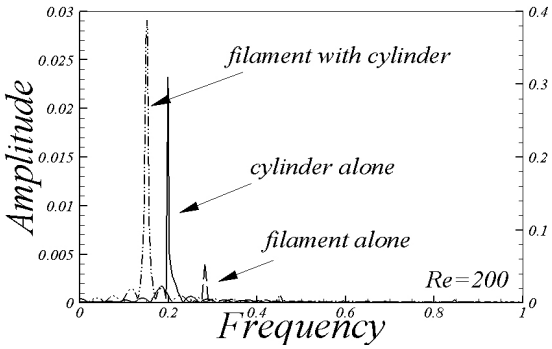

Fig. 7 Frequency spectrum of the lift coefficient at Re=200

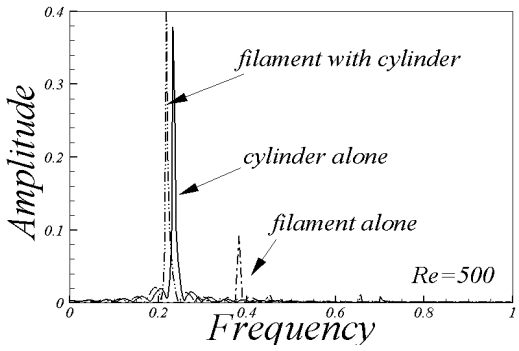

Fig. 8 Frequency spectrum of the lift coefficient at Re=500. The magnitude for filament alone is increased 10 times for clarity

that of Re=200.

Fig. 7 shows the frequency spectrum of the lift coefficient at Re=200. The interesting phenomenon lies that the magnitude of cylinder alone is considerably larger than filament with cylinder. The reason is that the vortex behind the cylinder in case of filament with cylinder is not detached from the cylinder before the vortex encounters the filament while the vortex behind the cylinder in case of cylinder alone is shedding from the cylinder. The frequncy for filament with cylinder is slightly lower than that of cylinder along and the frequncy for filament along is much higher than the other two. When the Reynolds number is increased to Re=500 (Fig. 8), we can interestingly see that the magnitude of cylinder alone is almost the same as filament with cylinder, indicating that the filament flapping is passively induced the vortex street behind the cylinder and the shedding frequency is affected very slightly by the filament. At Re=500, the vortex induced by cylinder is also shedding from the cylinder in case of filament with cylinder.

Fig. 9 shows the Strouhal number as a function of Reynolds number for filament with cylinder as well as cylinder alone and filament alone. The Strouhal number (St) is defined as fD/U_∞,

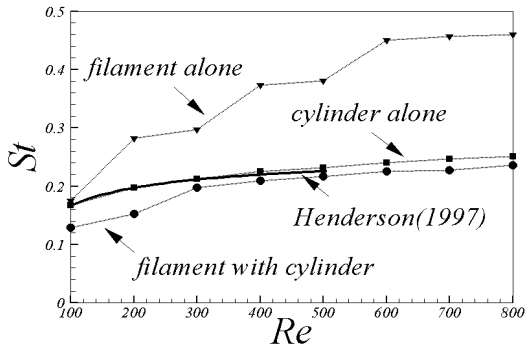

Fig. 9 Comparison of Strouhal number of filament with cylinder and that of cylinder alone as well as filament along at different Reynolds numbers

where f denotes the frequency of filament flapping and D is the cylinder width. The present results of cylinder alone are compared with previous studies[12] for validation and we can see a good agreement. As increasing Reynolds number, the Strouhal number of cylinder alone is almost the same as that of filament with cylinder. Jia et al.[7] showed that when arranged in tandem, the downstream filament flapped at the same frequency as that of the upstream one, but with a larger amplitude. Until Re=300, the Strouhal number of filament with cylinder is smaller than that of cylinder alone. The reason is that the vortex induced by cylinder in case of filament with cylinder is not detached from the cylinder before the vortex encounters the filament. The Strouhal number in case of filament alone is the highest compared with the other two. Only the tail part of filament is flapping with cylinder because the length is long, as also reported in Zhang et al.[2].

4. CONCLUSIONS

In this study, numerical simulations of energy harvesting eel by using the immersed boundary method have been carried out at different Reynolds numbers. The fluid motion is described by Eulerian variables defined on a fixed cartesian mesh, while the filament motion is described by Lagrangian variables defined on a freely moving mesh. Their interaction force was calculated explicitly using a feedback law. The transformation between the Eulerian and Lagrangian variables was established by a smoothed approximation of the Dirac delta function. In the case of cylinder alone, our result was in a good agreement with the previous study. The vortex behind the cylinder is not detached from the cylinder before the vortex encounters the filament at Re=200, while the vortex induced by cylinder is shedding from the cylinder at Re=500. The filament flapping at Re=500 is more

energetic with the larger amplitude for the fore part. The frequency spectrums of the lift coefficient for Re=200 and Re=500 were presented. The amplitude of filament with cylinder is considerably increased when Reynolds number increases from Re=200 to Re=500, because the vortex induced by cylinder is shedding from the cylinder at Re=500. As increasing Reynolds number, the strouhal number of cylinder alone is almost the same as that of filament with cylinder, indicating that the filament flapping is passively induced by the vortical structures behind the cylinder.

REFERENCES

[1] 2003, Muller, U., "Fish 'n Flag," *Science*, Vol.302, pp.1511-1512.

[2] 2000, Zhang, J., et al., "Flexible filaments in a flowing soap film as a model for one-dimensional flags in a two-dimensional wind," *Nature*, Vol.408, pp.835-839.

[3] 2002, Zhu, L. and Peskin, C.S., "Simulation of a flapping flexible filament in a flowing soap film by the immersed boundary method," *Journal of computational physics*, Vol.179, pp.452-468.

[4] 2000, Huber, G., "Swimming in Flatsea," *Nature*, Vol.408, pp.777-778.

[5] 2007, Huang, W.-X., et al., "Simulation of flexible filaments in a uniform flow by the immersed boundary method," *Journal of computational physics*, Vol.226, pp.2206-2228.

[6] 2003, Liao, J., et al., "Fish Exploiting Vortices Decrease Muscle Activity," *Science*, Vol.302, pp.1566-1569.

[7] 2008, Jia, L.-B. and Yin, X.-Z., "Passive Oscillations of Two Tandem Flexible Filaments in a Flowing Soap Film," *Physical review letters*, Vol.100, pp.228104(4).

[8] 2001, Taylor, G., et al., " The Energy Harvesting Eel: A Small Subsurface Ocean/River Power Generator," *IEEE journal of ocean engineering*, Vol.26, pp.539-547.

[9] 2001, Allen, J., et al., "ENERGY HARVESTING EEL," *Journal of fluids and structures*, Vol.15, pp.629-640.

[10] 2002, Kim, K., et al., "An implicit velocity decoupling procedure for incompressible Navier-Stokes equations," *Int. J. Numer. Meth. Fluids*, Vol.38, pp.125-138.

[11 2008, Huang, W.-X. and Sung, H.J., "Three-Dimensional Simulation of a Flapping Flag in a Uniform Flow," *Journal of Fluid Mechanics*, submitted.

[12] 1997, Henderson, R., "Nonlinear dynamics and pattern formation in turbulent wake transition," *Journal of Fluid Mechanics*, Vol.352, pp.65-112.